

Dear author,

Please note that changes made in the online proofing system will be added to the article before publication but are not reflected in this PDF.

We also ask that this file not be used for submitting corrections.

Two-photon conversion of a bacterial phytochrome

Serge G. Sokolovski,¹ Evgeny A. Zhrebtsov,^{2,3} Rajiv K. Kar,⁴ David Golonka,⁵ Robert Stabel,⁵ Nikolai B. Chichkov,¹ Andrey Gorodetsky,^{6,7,8} Igor Schapiro,⁴ Andreas Möglich,^{5,*} and Edik U. Rafailov^{1,*}

¹Optoelectronics and Biomedical Photonics Group, AIPT, Aston University, Birmingham, United Kingdom; ²Optoelectronics and Measurement Techniques, University of Oulu, Oulu, Finland; ³Cell Physiology and Pathology Laboratory, Orel State University, Orel, Russia; ⁴Institute of Chemistry, The Hebrew University of Jerusalem, Jerusalem, Israel; ⁵Photobiochemistry, University of Bayreuth, Bayreuth, Germany; ⁶Faculty of Physics and Engineering, ITMO University, St. Petersburg, Russia; ⁷Department of Chemistry, Imperial College London, London, United Kingdom; and ⁸School of Physics and Astronomy, University of Birmingham, Birmingham, United Kingdom

ABSTRACT In nature, sensory photoreceptors underlie diverse spatiotemporally precise and generally reversible biological responses to light. Photoreceptors also serve as genetically encoded agents in optogenetics to control by light organismal state and behavior. Phytochromes represent a superfamily of photoreceptors that transition between states absorbing red light (Pr) and far-red light (Pfr), thus expanding the spectral range of optogenetics to the near-infrared range. Although light of these colors exhibits superior penetration of soft tissue, the transmission through bone and skull is poor. To overcome this fundamental challenge, we explore the activation of a bacterial phytochrome by a femtosecond laser emitting in the 1 μm wavelength range. Quantum chemical calculations predict that bacterial phytochromes possess substantial two-photon absorption cross sections. In line with this notion, we demonstrate that the photoreversible Pr \leftrightarrow Pfr conversion is driven by two-photon absorption at wavelengths between 1170 and 1450 nm. The Pfr yield was highest for wavelengths between 1170 and 1280 nm and rapidly plummeted beyond 1300 nm. By combining two-photon activation with bacterial phytochromes, we lay the foundation for enhanced spatial resolution in optogenetics and unprecedented penetration through bone, skull, and soft tissue.

SIGNIFICANCE Sensory photoreceptor proteins mediate vital physiological adaptations to light. In optogenetics, they serve as light-gated actuators to enable the control of cellular state and physiology with precision in time and space. The application of optogenetics to entire organisms, especially within the brain, remains challenging, to a large extent owing to poor penetration of visible light through tissue and bone. To address this fundamental challenge, we investigate here the actuation of a bacterial phytochrome photoreceptor via two-photon (2P) absorption of femtosecond laser radiation of micrometer wavelengths. 2P absorption drives the bidirectional photoconversion between two activity states of the phytochrome. By principally demonstrating the validity of 2P actuation, our study paves the way toward optogenetic applications with enhanced penetration depth and spatial resolution.

Q3 Q4 Q5 INTRODUCTION Q1 Q2

Light-dependent adaptations of physiology, behavior, and development in nature are mediated by sensory photoreceptor proteins (1,2). Sensitivity to specific bands of the electromagnetic spectrum is provided by chromophores, small aromatic compounds embedded within the photoreceptor. The light-dependent responses elicited by sensory photoreceptors generally exhibit characteristic hallmarks: they are precise in time and space, they are reversible, and they are fully genetically encoded. For precisely these traits,

sensory photoreceptors double as actuators for the manipulation by light of cellular state and physiology in optogenetics (3). Originating in the neurosciences, optogenetics Q6 has become a powerful approach across many areas of biology, allowing scientists to tackle unresolved questions in unprecedented ways. Although initially, optogenetics was confined to a small set of naturally occurring opsin photoreceptors, foremost the ion-conducting channelrhodopsins (4,5), since then the repertoire of available actuators has been greatly expanded by other photoreceptor classes and by protein engineering. In this manner, a multitude of cellular processes have been unlocked for optogenetic intervention beyond the opsin-based control of the ion distribution across the plasma membrane (6). Despite these advances, the application of optogenetics in the brain of living animals remains demanding. To surmount these

Submitted October 16, 2020, and accepted for publication January 7, 2021.

*Correspondence: andreas.moeglich@uni-bayreuth.de or e.rafailov@aston.ac.uk

Editor: Andrew Plested.

<https://doi.org/10.1016/j.bpj.2021.01.028>

© 2021 Biophysical Society.

challenges, there has been a push toward actuators that can be activated more effectively because they respond to longer wavelengths with better tissue penetration (7,8), they exhibit extended lifetimes of their active states (9), or both. Phytochrome photoreceptors (Phys) in principle provide a viable alternative because they intrinsically respond to longer wavelengths than opsins do and thereby expand the spectrum available for optogenetic actuation into the red and near-infrared region (10). Light within this region falls in the near-infrared spectral window and displays enhanced penetration of soft tissue (11), thereby rendering phytochromes attractive for optogenetics.

First discovered in land plants (12), phytochromes are a class of sensory photoreceptors that underpin manifold adaptive responses to red and near-infrared light across plants, algae, bacteria, and fungi (13,14). At the molecular level, Phys generally exhibit bipartite architecture with an N-terminal photosensory core module (PCM) that processes light signals and a C-terminal output module that exerts downstream physiological responses (Fig. 1 a). The Phy PCM generally consists of serial PAS (Per-ARNT-Sim (15)), GAF (cGMP-specific phosphodiesterase, adenylyl cyclase and FhlA (16)), and PHY (PHY-specific (17,18)) domains. To enable absorption of light in the red to near-infrared spectral range, Phys covalently bind within their GAF domains linear tetrapyrrole (i.e., bilin) chromophores (Fig. 1 b). Phys cycle between two states, denoted Pr and Pfr, that absorb red and far-red light, respectively, and that differ in the configuration of their chromophore. Within the Pr state, the bilin chromophore assumes the Z isomer of its C15 = C16 double bond. Absorption of red light drives the Pr → Pfr transition, which is characterized by bilin isomerization to the 15E state, and far-red light promotes the reverse Pfr → Pr reaction. In conventional Phys, the Pr state is thermodynamically more stable than Pfr and prevails in darkness. By contrast, the so-called bathyphytochromes assume the Pfr form as their dark-adapted state. The 15Z/E isomerization underlying the Pr → Pfr transition triggers the refolding of a protrusion of the PHY domain, termed the PHY tongue, from a β-hairpin to an α-helical conformation and thereby induces quaternary structural rearrangements within the homodimeric Phy PCM (19–21). The nature and mode of action of the output module differ between bacterial and plant Phys. In bacterial Phys (BPhys), the output module comprises effector units that directly mediate the biological output, often enzymatic in nature. By contrast, plant Phys generally elicit physiological responses through light-dependent nuclear translocation, protein degradation, and protein-protein interactions with intracellular partners, particularly the phytochrome-interacting factors (22–25). Bacterial and plant Phys further differ in the type and attachment site of their bilin chromophores. Whereas BPhys covalently attach biliverdin (BV) to a cysteine at the PAS N-terminus, plant Phys incorporate a derivative of BV, phytychromobilin, bound to a cysteine

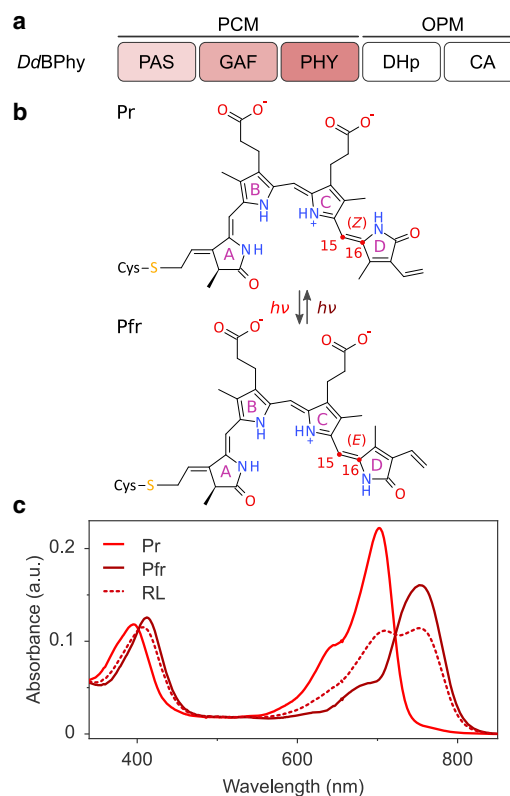


FIGURE 1 Architecture and photochemistry of the *D. deserti* bacteriophytochrome (*DdBPhy*). (a) *DdBPhy* consists of a photosensory core module (PCM) with consecutive PAS, GAF, and PHY domains and of an output module (OPM) that comprises DHp and CA domains and acts as a histidine kinase. (b) In darkness, the *DdBPhy* PCM predominantly adopts the red-absorbing Pr state with the biliverdin chromophore in its 15Z conformation. Red light drives isomerization to the 15E conformation, leading to the population of the far-red-absorbing Pfr state. Far-red (or near-infrared) light drives the reverse Pfr → Pr reaction. (c) Pr and Pfr absorbance spectra of the *DdBPhy* PCM are shown. The dashed line (RL) denotes the mixed-state spectrum obtained at the photostationary state under illumination with red light ((680 ± 15) nm).

within the GAF domain (13). Because of the more extended conjugated π electron system of BV, BPhys exhibit a bathochromic shift of their Pr and Pfr states relative to those of plant Phys. Moreover, BV widely occurs in mammalian tissue (26–30), unlike phytychromobilin or the cyanobacterial phycocyanobilin that plant Phys can also accommodate.

Both bacterial and plant Phys have witnessed use in optogenetics (31). Of particular advantage, the bimodal toggling of Phys between (meta)stable states of different activity by two light colors can be leveraged for enhanced optogenetic resolution in time and space (32). Because Phys respond to comparatively long wavelengths, they can be actuated within the near-infrared spectral window in which light exhibits superior soft tissue penetration (11). Owing to the availability of BV in mammals (26,29,33), BPhys are principally suitable for in vivo optogenetics in living animals. To this end, several BPhys-based optogenetic actuators have been built by protein engineering (10,31). On the one

hand, a collection of BPhy receptors (27,29,30,34) act as photoactivated nucleotidyl cyclases and catalyze the formation of cyclic mono- and dinucleotides that serve as second messengers in eukaryotes and prokaryotes. In a similar vein, we constructed light-activated BPhy-phosphodiesterases that hydrolyze cyclic mononucleotides (26,35). On the other hand, certain BPhy receptors enter light-dependent protein-protein interactions that have been harnessed to optogenetically control subcellular localization and gene expression (36,37).

Although phytochromes respond to comparatively long wavelengths and exhibit bimodal Pr \leftrightarrow Pfr switching, their optogenetic deployment in the brain remains challenging, particularly owing to limited skull and bone penetration of visible to near-infrared light. To overcome this restriction and to thus enable transcranial actuation of phytochrome photoreceptors, we envision nonlinear activation of phytochromes by a femtosecond pulsed laser with near-infrared wavelengths of 1000–1450 nm (38). Notably, light of these wavelengths offers better penetration through the skull (39,40), thus significantly increasing the accessible depth in brain tissue. Two-photon (2P) excitation was previously applied to a set of modified bacterial phytochrome variants to evoke fluorescence (41), thus demonstrating that phytochromes can be optically excited in a nonlinear regime. However, these studies focused on incapacitated receptors optimized for enhanced fluorescence quantum yield but impaired in their photochemistry. As a corollary, the experiments did not uncover whether Pr \rightarrow Pfr photoconversion, as opposed to fluorescence, can be driven by 2P irradiation and, if so, to what extent. To assess these fundamental aspects and thereby gauge the principal feasibility of nonlinearly activating phytochrome receptors, we investigated here the actuation of a bacterial Phy in the two-photon regime (42–45).

MATERIALS AND METHODS

Molecular biology and protein expression

The gene encoding the *Deinococcus deserti* photosensory core module (*DdPCM*) (WP_012695070.1, residues 1–520) was synthesized with *Escherichia coli*-adapted codon usage (GeneArt, Regensburg, Germany) and cloned into a pCDFDuet plasmid (Novagen, Merck, Darmstadt, Germany) with a C-terminal hexahistidine tag via Gibson assembly (46). The gene encoding *Synechocystis* sp. heme oxygenase 1 (*SsHO*) was amplified by PCR from plasmid pKT270 (47) and cloned by Gibson assembly into the pCDFDuet vector, such that the expression of *DdPCM* and *SsHO* is under control of T7-lacO promoters. The integrity of the construct was confirmed by Sanger DNA sequencing (Microsynth Seqlab, Göttingen, Germany). For expression, the plasmid was transformed into BL21(DE3) cells and used to inoculate two baffled flasks with 800 mL lysogeny broth medium supplemented with 100 $\mu\text{g mL}^{-1}$ streptomycin. Bacterial cultures were grown at 37°C and 225 rpm up to an optical density at 600 nm of around 0.6, at which point the temperature was lowered to 16°C and 0.5 mM δ -amino levulinic acid was added. Expression of *DdPCM* and *SsHO* was induced by addition of 1 mM isopropyl β -D-1-thiogalactopyranoside, and cultivation continued at 16°C and 225 rpm for 16 h. Purification of *DdPCM* was con-

ducted similarly to previous protocols (26,35). In brief, cells were spun down, resuspended in 50 mM Tris/HCl (pH 8.0), 20 mM NaCl, 20 mM imidazole, and supplemented with protease inhibitors (cOmplete Ultra; Roche Diagnostics, Mannheim, Germany). After lysis by microfluidizer and centrifugation, the supernatant was incubated for 1 h at 4°C with 100 μM biliverdin hydrochloride (Livchem Logistics, Frankfurt, Germany) and 5 mM Tris-(2-carboxyethyl)-phosphine. The lysate was then applied to Ni²⁺-nitrilotriacetic acid affinity resin (Protino Ni-NTA; Macherey and Nagel, Düren, Germany). After extensive washing of the resin, the bound protein was eluted with 200 mM imidazole, pooled, and dialyzed into 50 mM Tris/HCl (pH 8.0), 20 mM NaCl. After purification by anion-exchange chromatography (HiTrap Q HP; GE Healthcare, Munich, Germany), the protein purity was analyzed by denaturing polyacrylamide gel electrophoresis and Coomassie staining. Covalent chromophore incorporation was assessed by Zn²⁺-induced bilin fluorescence (48). Fractions containing pure protein were pooled, dialyzed into storage buffer (50 mM Tris/HCl (pH 8.0), 20 mM NaCl, 20% (w/v) glycerol) and concentrated by spin filtration (Vivaspin 6, 10-kDa cutoff; GE Healthcare). Sample concentration was determined by absorbance measurements (8453 ultraviolet-visible (UV-vis); Agilent Technologies, Waldbronn, Germany) based on an estimated molar extinction coefficient of 45,700 M⁻¹ cm⁻¹ at the isosbestic point (724 nm) (26). For storage, protein aliquots were flash frozen in liquid nitrogen and stored at -80°C.

UV-vis absorbance spectra of *DdPCM* were recorded on an Agilent 8435 diode-array spectrophotometer (Agilent Technologies) for dark-adapted *DdPCM* and after irradiation with red ((680 \pm 15) nm, 80 $\mu\text{W cm}^{-2}$) or far-red light ((780 \pm 15) nm, 80 $\mu\text{W cm}^{-2}$) for 30 s. The spectrum of the pure Pfr state was calculated according to (49). Pfr \rightarrow Pr recovery kinetics were recorded on a Cary 100 UV-vis spectrophotometer (Agilent Technologies) by following absorbance over time at 703, 722, and 755 nm after saturating illumination with red light. Data were evaluated and plotted with the Fit-o-mat program (50).

Computational methods

A homology model of *DdPCM* in the Pr dark-adapted state was generated as a starting point for the computational work. The amino acid sequence of *DdPCM* was retrieved from the UniProt Database (C1D3W9) and compared with related sequences using Swiss-Model (51). The x-ray crystal structure of the BPhy (chain A with a sequence identity of 48%) from *D. radiodurans* (*DrPCM*) at a resolution of 2.75 Å (Protein Data Bank, PDB: 4Q0J) (52) was selected as the template. The homology model was assessed using MolProbity, which evaluates various aspects such as atomic clashes, side chain rotamers, and Ramachandran angles and is normalized to be on the same scale as x-ray resolution (53,54). The obtained score of 1.36 corresponds to the 97th percentile and indicates a high-quality model (the 100th percentile is considered the best structure). In addition, the homology model was also inspected visually by overlaying the structure of the BV chromophore binding pocket of the *DrPCM* and the *DdPCM* (Fig. S2). Water molecules from the template structure (4Q0J) were copied into the homology model and relaxed in the molecular mechanics (MM) region during optimization.

The homology model was solvated with TIP3P water models in a rectangular box with a distance of at least 13.5 Å from any protein atom to the boundary of the box. quantum mechanics (QM)/MM geometry optimization was performed using ChemShell interfaced to the Orca 4.1 program (55). The amino acids and water molecules constitute the MM region and were described using the Amber ff14SB force field (56). A hydrogen link atom was placed between the C-C atom of the BV chromophore, after the sulfur atom of the covalently linked Cys residue. The QM region was treated at the BLYP/cc-pVDZ level of theory, with D3BJ dispersion correction in the geometry optimization (57). This method was chosen based on the previous benchmark for the linear tetrapyrrole chromophore such as found in phytochromes (57).

The calculation of one-photon absorption (1PA) was done for the 10 lowest excited states. Here, we used the approximate coupled cluster method CC2 with the “resolution of identity” (RI) as implemented in Turbomole 7.3 (58). The basis set aug-cc-pVDZ and the corresponding auxiliary basis set were used, with frozen core orbitals by default. The surrounding environment was treated as point charges.

To further assess the reliability of our approach, the 1PA and 2PA calculations were performed on two different sizes of the QM region, as shown in Fig. 2. The smaller QM region (QM65) consists of the BV chromophore with truncated propionate side chains, thus comprising 65 atoms including two additional link atoms to account for the truncation of propionate chains. The larger QM region (biliverdin comprising 75 atoms) additionally contains the propionates and is identical to the one used for the geometry optimization. The two-photon absorption (2PA) calculations were performed for the first excited state, at the same level of theory. Estimation of the 2PA cross section was based on Eq. 1, as illustrated by Beerepoot et al. (59).

$$\sigma^{TPA} = \frac{N\pi^3\alpha\alpha_0^5\omega^2}{c} \langle \delta^{TPA} \mathbf{g} \rangle (2\omega, \omega_0, \Gamma), \quad (1)$$

where N is the integer number, α is the fine structure constant, α_0 is the Bohr radius, ω is the photon energy, c is the speed of light, $\langle \delta^{TPA} \mathbf{g} \rangle$ is the rotationally averaged two-photon transition moment, and $g(2\omega, \omega_0, \Gamma)$ is the line shape function. Considering the experimental setup, $N = 4$ and $\Gamma = 0.2$ eV (full-width half maximum) were used in Eq. 1.

Quantitative modeling of two-photon photoconversion

The transformation of *DdPCM* by two-photon irradiation was modeled by considering the fractions R and FR of the Pr and Pfr state within the focal volume. During illumination, R and FR change over time t according to

$$dR/dt = -k_1 \times R + k_{-1} \times FR + D \times (R_0 - R) \quad (2)$$

and

$$dFR/dt = k_1 \times R - k_{-1} \times FR + D \times (FR_0 - FR), \quad (3)$$

where k_1 and k_{-1} are unimolecular rate constants for the light-driven Pr \rightarrow Pfr and Pfr \rightarrow Pr transitions, respectively; the diffusion constant D ac-

counts for diffusion of molecules into and out of the focal volume; and R_0 and FR_0 are the fractions of the Pr and Pfr states in the absence of illumination. Accounting for the two-photon absorption, the velocities of both transitions are assumed to quadratically depend on the photon flux Φ according to

$$k_1 = f_1 \times \Phi^2 \quad (4)$$

and

$$k_{-1} = f_{-1} \times \Phi^2 \quad (5)$$

The photon flux is proportional to the applied laser power P according to

$$\Phi = g_\lambda \times P, \quad (6)$$

where the coefficient g_λ considers the relative energy content and flux density of the photons of the different wavelengths used. Normalized to the value at 1190 nm, the coefficients were $g_{1190} = 1$, $g_{1250} = 0.96$, and $g_{1310} = 0.91$.

By integration of Eqs. 2 and 3, the expression Eq. 4 is obtained for the fraction FR inside the laser focal volume at time t :

$$FR(t) = R_0 + FR_0 - R_\infty - (R_0 - R_\infty) \times \exp(-\tilde{k} \times t), \quad (7)$$

where

$$\tilde{k} = k_1 + D + k_{-1} \quad (8)$$

and

$$R_\infty = k_{-1}/\tilde{k} \times (R_0 + FR_0) + D/\tilde{k} \times R_0 \quad (9)$$

At the photostationary state, the fraction of FR is hence given by

$$FR_\infty = R_0 + FR_0 - k_{-1}/\tilde{k} \times (R_0 + FR_0) + D/\tilde{k} \times R_0 \quad (10)$$

Notably, the steady-state value FR_∞ depends on the ratio of the rate constants D , k_1 , and k_{-1} rather than their individual values. The rate constants were hence taken as dimensionless, and D was fixed at an arbitrary value of 1. The two-photon power-dependence data at wavelengths of 1190, 1250, and 1310 nm were globally fitted with Fit-o-mat (50) using the individual parameters f_1 and f_{-1} . Fitted parameters were $f_1^{1190} = (1.1 \pm 0.2) \times 10^{-2} \text{ mW}^{-2}$, $f_{-1}^{1190} = (2.0 \pm 0.4) \times 10^{-2} \text{ mW}^{-2}$, $f_1^{1250} = (6.9 \pm 1.0) \times 10^{-3} \text{ mW}^{-2}$, $f_{-1}^{1250} = (1.0 \pm 0.2) \times 10^{-2} \text{ mW}^{-2}$, $f_1^{1310} = (1.4 \pm 0.4) \times 10^{-2} \text{ mW}^{-2}$, and $f_{-1}^{1310} = (5.3 \pm 2.0) \times 10^{-2} \text{ mW}^{-2}$.

RESULTS

Among the first-described bacterial phytochromes (60–62), the BPhy from *D. radiodurans* has been widely studied in terms of function, photochemistry, mechanism, and structure (19,20,63–65). As a consequence, a set of engineered photoreceptors are based on the *DrPCM*, especially for the regulation of cyclic mononucleotides (26,29,30). However, several of these receptors suffered from impaired light-dependent regulation, in that far-red light could not fully counteract prior activation by red light. In the context

Web 3C

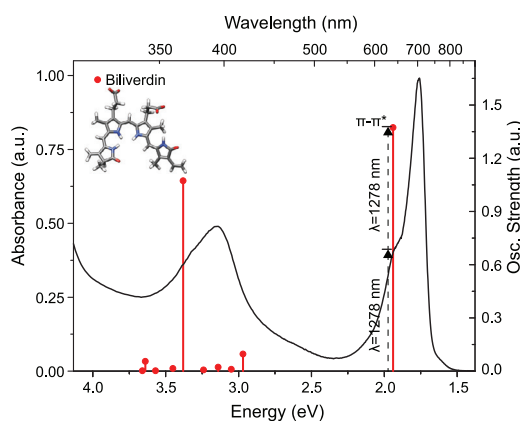


FIGURE 2 The experimentally measured Pr absorbance spectrum of the *DdPCM* (black line) and the calculated vertical excitation energies in stick representation. The height of the sticks is determined by the oscillator strength. The two-photon excitation energy is marked as a dashed stick. The optimized geometry of the biliverdin chromophore is shown in the inset. To see this figure in color, go online.

of a photoactivated adenylyl cyclase (27), we recently found that fully photoreversible, bidirectional switching of enzymatic activity could be attained via exchange of the *DrPCM* for the homologous PCM of *DdPCM*. Although the underlying molecular reasons remain elusive, *DdPCM* evidently improved the performance, and therefore, we focused on this variant. To this end, we heterologously expressed the *DdPCM* in *E. coli* and analyzed it by UV-vis spectroscopy (Fig. 1 c). In its dark-adapted state, *DdPCM* predominantly adopted its Pr form, characterized by Soret and Q absorption bands at around 390 and 700 nm, respectively. Irradiation with red light ((680 ± 15) nm) partially populated the Pfr state with a Q-band absorption around 750 nm. Notably, under saturating 680-nm light, a steady-state Pfr/Pr mixture of 0.69:0.31 was achieved (Fig. 1 c, dashed line). Put another way, light drives both the Pr → Pfr and the Pfr → Pr transitions, and a photostationary state is reached. Subsequent exposure to far-red light ((780 ± 15) nm) restored the original dark-adapted spectrum. We next monitored the thermal recovery to the dark-adapted Pr state after prior exposure to red light. At 22°C, the slow recovery kinetics could be fitted by a sum of two exponential functions with rate constants of $k_1 = (1.60 \pm 0.01) \times 10^{-2} \text{ min}^{-1}$ and $k_2 = (2.01 \pm 0.01) \times 10^{-4} \text{ min}^{-1}$ (Fig. S1).

Quantum chemical calculation of two-photon absorption

We next calculated electronic excitation spectra for the *DdPCM* to assess nonlinear actuation by two-photon irradiation. Because no high-resolution structure is available yet for *DdPCM*, we generated a homology model for the dark-adapted Pr state based on the structure of the *DrPCM* (Fig. S2; (52)). Using the hybrid QM/MM method, we first calculated 1PA spectra of the Pr form of *DdPCM* (Fig. 2). In the simulations, the QM region either encompassed all atoms of the biliverdin chromophore or excluded the propionate side chains (QM65). This choice is justified by the analysis of the molecular orbitals involved in the electronic transitions (Fig. S3), which are localized exclusively on the four pyrrole rings. Hence, the electronic transitions do not involve the propionate side chains because they are not a part of the conjugated π electron system. This signifies that the size of QM region, or more specifically the inclusion of the propionate chains, has no impact on the absorbance peaks.

The excitation energy for the $S_0 \rightarrow S_1$ transition, corresponding to the Q band, is found at 1.94 eV (642 nm). This value overestimates the experimental one of 1.77 eV (700 nm) by 0.17 eV, well within the error range of the method (66). The excitation energy for the transition that gives rise to the Soret band is found at 3.38 eV (368 nm), consistently overestimating the experimental peak at 3.18 eV (390 nm) by 0.2 eV. In these simulations, the Q band constitutes transition to the S_1 state, and the Soret band cor-

responds to that to the S_6 state. There are, however, additional excited states between the Q and Soret bands that have very small oscillator strength and are hence called dark states (Fig. 2). The shoulder of the Soret band is due to the vibronic coupling, as evidenced by experiments and simulation (67). This is also confirmed by our simulation because no additional excited state close to S_1 was found. The full description of the excited states, the oscillator strengths, and the frontier orbitals are provided in Table S1. The oscillator strength of the transitions correlates with the relative intensities of the corresponding Soret and Q bands in the experimental spectrum (Table 1).

We then calculated the 2PA energy for the first bright state as summarized in Table 1. To this end, we used the RI-CC2 method, which has been assessed for the calculation of 2PA of protein-embedded chromophores (59,68). The calculated 2PA energies are degenerate in nature and correspond to half of the excitation energy obtained from 1PA calculations. δ^{TPA} corresponds to the two-photon transition moment and is directly proportional to the 2PA cross section (σ^{TPA}) in GM (Goeppert Mayer) units. δ^{TPA} was 6757 arbitrary units (au), and the calculated σ^{TPA} obtained from the simulation was 9.309 GM. Taken together, the QM/MM calculations predict that the *DdPCM* can be actuated by 2PA with energies around 0.97 eV, corresponding to a wavelength of 1278 nm. Notably, the truncation of the propionate side chains has no significant effect on the calculated vertical excitation energies (Fig. S4; Table S2; Supporting materials and methods).

Two-photon conversion of *DdPCM*

We experimentally tested and characterized the effect of nonlinear activation of *DdPCM* by a femtosecond pulsed laser emitting between 1170 and 1450 nm. To this end, we developed an optical setup (Fig. 3) that integrates linear one-photon and nonlinear two-photon (2P) irradiation and allows the confocal measurement of absorbance changes. We used an optical parametric amplifier (TOPAS Prime; Coherent, Santa Clara, CA) pumped with a Ti:sapphire laser (Astrella; Coherent) to deliver pulses of ~50 fs width at a repetition rate of 4 kHz, tunable wavelengths between 1170 and 1450 nm and average optical powers up to ~50 mW (peak power ~235 MW). After passing through a dichroic mirror, the femtosecond laser pulses are reflected

TABLE 1 Calculated 1PA and 2PA excitation energies for the Q and Soret bands

Biliverdin	1PA		2PA	
	Energy (eV)	Oscillator strength (<i>f</i>)	Energy (eV)	δ^{TPA} (au) σ^{TPA} (GM)
Q band	1.94	1.374	0.97	6757 9.309
Soret band	3.38	1.074		

The calculations were performed at the RI-CC2/aug-cc-pVDZ level of theory.

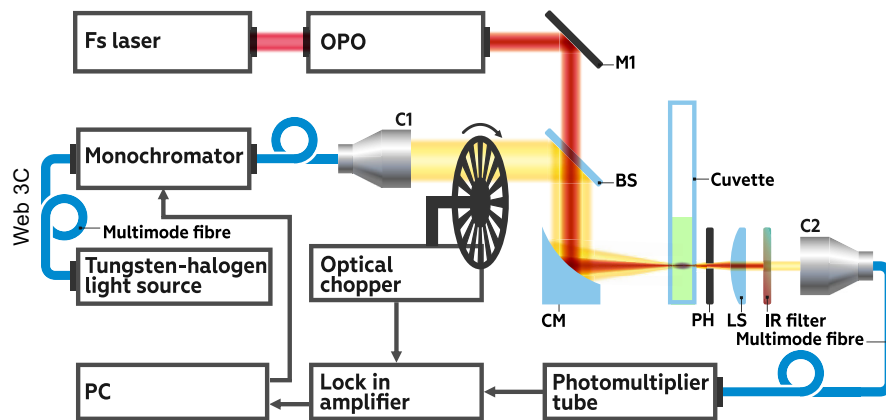


FIGURE 3 Schematic representation of the instrumental setup consisting of a subsystem for two-photon phytochrome activation at 1170–1450 nm spectral range and a channel for confocal absorbance measurements in the spectral range of 550–810 nm. Abbreviations are BS, dichroic mirror; C1 and C2, collimators; CM, concave mirror; LS, collecting lens; M1, mirror; OPO, optical parametric oscillator; PH, pinhole. To see this figure in color, go online.

from a concave mirror ($f = 200$ mm, radius of curvature 400 mm) and thereby focused on a spot inside a sample cuvette of 1 mm thickness. To measure absorbance changes associated with the phytochrome Pr \rightarrow Pfr transformation within the focal area, we implemented synchronous, confocal detection by ultra-low-power probe radiation in the spectral range of 550–810 nm. To this end, the probe beam was collimated and coaligned with the micrometer laser radiation via the dichroic mirror and two pinholes placed after and at the center position of the cuvette. After the alignment, the latter pinhole was removed, and the cuvette holder was installed. The collecting lens and the collimator gathered the transmitted probe light, and an infrared filter prevented the laser beam from hitting the photomultiplier detector.

For the measurements, we used a *DdPCM* concentration of 50 μ M. The temperature inside the cuvette was monitored by a miniature thermocouple placed near the focal spot. Notably, measurements by the thermocouple might hence somewhat underestimate the actual temperature increase within the focal spot. In a control experiment using the highest laser power of 50 mW, the temperature increase was less than 2°C. To initially toggle the phytochrome between its Pr and Pfr forms, we exposed the cuvette to LEDs emitting at 766 and 680 nm, respectively (Fig. 4 a). Using these LEDs to drive the linear Pr \leftrightarrow Pfr photoconversion, the sample integrity could be assessed between measurements and the *DdPCM* could be transformed to its Pr state for subsequent nonlinear photoconversion. To this end, we subjected the sample in its Pr state to the femtosecond laser pulses and recorded the resultant absorbance changes immediately afterwards. In line with an earlier report (41), the laser radiation elicited fluorescence of the sample. Upon irradiation with laser pulses in the spectral range of 1170–1450 nm for 1 min, the *DdPCM* samples exhibited characteristic absorbance changes (Fig. 4 a), with the peak at around 700 nm decreasing and a new one forming at around 750 nm. Based on comparison with the absorbance spectra of *DdPCM* in its Pr and Pfr states (see Fig. 1 c), we assign these changes as Pr

\rightarrow Pfr conversion of the phytochrome molecules by multiphoton absorption.

To verify that it is two-photon absorption that drives the Pr \rightarrow Pfr conversion of the *DdPCM*, we applied various power intensities. In the intensity regime below 10 mW, the yield of the Pfr state increased with power approximately quadratically (Fig. 4 b), which indicates that the Pr \rightarrow Pfr transition is induced by two-photon absorption. At higher powers above 10 mW, the Pfr yield approached a plateau (Fig. 4 c). Neither extending the time of irradiation nor increasing the power beyond \sim 10–20 mW enhanced the Pfr yield further. We next analyzed the wavelength dependence of the Pr \rightarrow Pfr conversion in the two-photon regime. To this end, we assessed to which extent illumination from 1170 to 1450 nm is capable of effectively transforming the *DdPCM* from its Pr to the Pfr state (Fig. 4 d). The Pr \rightarrow Pfr conversion remained relatively constant at around 35% over the range of 1170–1300 nm but plummeted to \sim 20% or lower for wavelengths above 1300 nm.

DISCUSSION

Our hybrid quantum mechanical/molecular mechanics simulations clearly suggest that *DdPCM* and, by extension, likely other bacterial phytochromes possess appreciable two-photon absorption cross sections in the micrometer wavelength range. In line with this notion, an earlier study demonstrated two-photon fluorescence for a set of bacterial phytochromes and thereby provided important benchmarks for their use as novel, genetically encodable fluorophores emitting in the red to near-infrared spectral range (41). However, the phytochromes under study were deliberately incapacitated in their Pr \rightarrow Pfr photoconversion so as to enhance fluorescence quantum yield. It thus remained unclear whether two-photon absorption can efficiently drive the Pr \rightarrow Pfr photoconversion. To fill this principal gap in our knowledge, we devised an optical setup that integrates pulsed, femtosecond two-photon excitation with confocal absorbance readout to assess the degree of photoconversion.

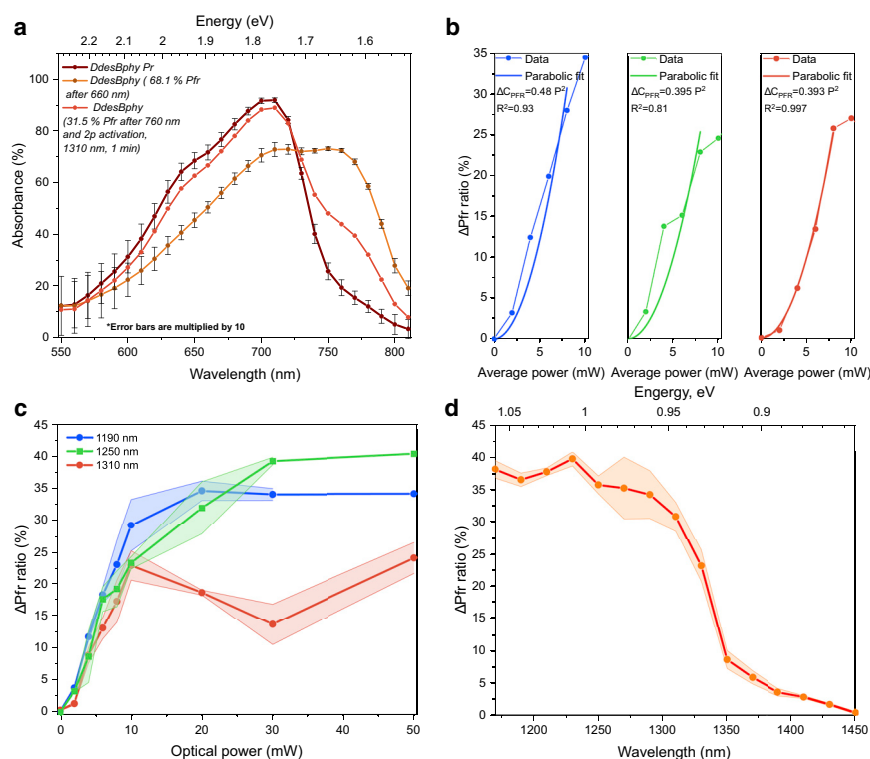


FIGURE 4 Nonlinear Pr \rightarrow Pfr photoconversion of *DdPCM*. (a) Absorbance spectra of *DdPCM* upon irradiation with 660-nm (yellow line) and 766-nm (dark red line) light are shown. The red line denotes the absorbance spectrum obtained after two-photon photoconversion using femtosecond laser irradiation at 1310 nm. (b) The amount of Pfr state generated by 2P photoconversion in the regime of lower optical powers at wavelengths of 1190 nm (blue), 1250 nm (green), and 1310 nm (red) is given. The lines represent fits to parabolic functions. (c) Power dependence of the two-photon photoconversion over a broader pump power range is shown. (d) Dependence of the maximal absorbance changes of *DdPCM* on 2P irradiation wavelength is shown.

Our data reveal that two-photon irradiation can not only elicit fluorescence in phytochromes, as reported earlier, but also drives their productive Pr \rightarrow Pfr photoconversion.

To arrive at a better understanding of the underlying processes and their implications, we sought to globally analyze the experimental data by a phenomenological mechanistic model of two-photon photoconversion (Fig. 5 a). The model considers three elementary reactions: 1) Pr \rightarrow Pfr photoconversion within the focal volume, 2) a process returning the Pfr state to Pr within the focal volume, and 3) diffusion between the focal volume and the considerably larger bulk volume. We modeled the forward Pr \rightarrow Pfr reaction as a two-photon process, based on principal considerations and supported by the approximately quadratic power dependence of photoconversion yields at lower intensities (Fig. 4 b). Whereas this process (reaction 1) evidently increases the Pfr amount inside the focal volume, diffusional exchange (reaction 3) with the surrounding bulk volume, which contains *DdPCM* fully in its Pr state, leads to a net decrease. The competition between reactions 1 and 3 (see Fig. 5 a) during 2P irradiation explains why at a given wavelength and power, the Pfr yield does not increase beyond a certain illumination time. Strikingly, our data revealed that the Pfr yield asymptotically approaches plateau values between 20 and 40%, depending on wavelength. This observation directly implies that there is a return process (reaction 2) that depletes the Pfr state. Moreover, the fact that a constant plateau is reached indicates that this return reaction has

the same power dependence on 2P irradiation intensity as the forward reaction 1. In analogy to the linear excitation regime in which red light exposure results in a photostationary Pr/Pfr mixture (see Fig. 1 c), we deem two-photon Pfr \rightarrow Pr photoconversion the most likely candidate for the return process 2.

To ascertain whether the experimental data conform to this mechanistic model, we globally analyzed them according to the reaction scheme in Fig. 5 a (see Materials and methods). The Pfr yield reached inside the focal volume at photostationary state, FR_{∞} , is given by Eqs. 11 and 12.

$$FR_{\infty} = R_0 + FR_0 - k_{-1}/\tilde{k} \times (R_0 + FR_0) + D/\tilde{k} \times R_0 \quad (11)$$

and

$$\tilde{k} = k_1 + D + k_{-1}, \quad (12)$$

where $R_0 = 1$ and $FR_0 = 0$ are the Pr and Pfr fractions in the absence of irradiation and k_1 , k_{-1} , and D denote the rate constants for the Pr \rightarrow Pfr photoconversion, the Pfr \rightarrow Pr reversion, and the diffusional exchange, respectively. The rate constants for the forward and reverse photoconversion k_1 and k_{-1} are taken to scale with the square of the photon flux Φ inside the focal volume, which in turn is related to the applied laser power P according to Eq. 13.

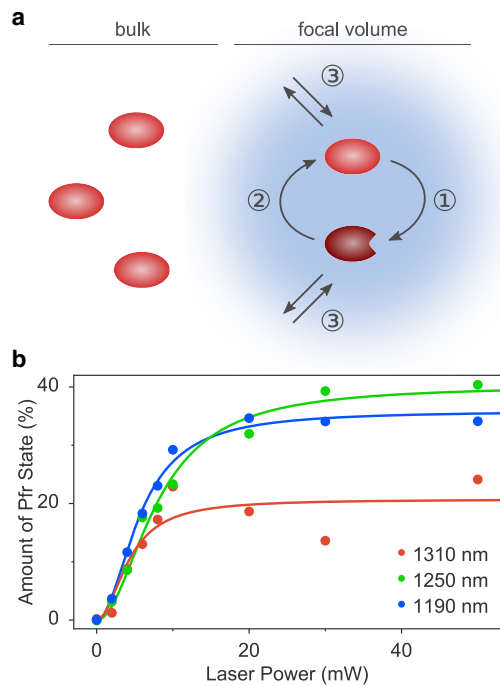


FIGURE 5 Quantitative analysis of two-photon photoconversion in *DdPCM*. (a) Reaction sequence under two-photon irradiation is given. Inside the focal volume, the *DdPCM* is converted from its initial Pr state (red ellipsoids) to its Pfr state (dark red) via two-photon photoconversion (process 1). The 2P irradiation simultaneously drives the Pfr \rightarrow Pr reverse process (2). During the experiment, *DdPCM* diffuses out of the focal volume into the surrounding, much larger bulk volume and vice versa (3). At the start of the experiment, the *DdPCM* resides completely in its Pr state. (b) The circles denote the experimental data from Fig. 4 c, and the solid lines represent a global fit to the model shown in (a).

$$\Phi = g_{\lambda} \times P, \quad (13)$$

where the constant g_{λ} accounts for the difference in relative photon energy and flux density within the focal volume for the individual wavelengths.

As is apparent from Eq. 11, the Pfr yield reached at photostationary equilibrium for a given wavelength and power does not depend on the absolute velocities k_1 , k_{-1} , and D of the individual reactions, but rather on their ratios. We hence fixed the diffusion rate constant at an arbitrary value of $D = 1$. A global fit of the power-dependency data at wavelengths of 1190, 1250, and 1310 nm then yielded parameter values of $k_1^{1190} = (1.1 \pm 0.2) \times 10^{-2} \text{ mW}^{-2} \times P^2$, $k_{-1}^{1190} = (2.0 \pm 0.4) \times 10^{-2} \text{ mW}^{-2} \times P^2$, $k_1^{1250} = (6.4 \pm 0.9) \times 10^{-3} \text{ mW}^{-2} \times P^2$, $k_{-1}^{1250} = (9.5 \pm 1.8) \times 10^{-3} \text{ mW}^{-2} \times P^2$, $k_1^{1310} = (1.1 \pm 0.4) \times 10^{-2} \text{ mW}^{-2} \times P^2$, and $k_{-1}^{1310} = (4.3 \pm 1.6) \times 10^{-2} \text{ mW}^{-2} \times P^2$ (Fig. 5 b). The fitted curves describe the data well, thus lending credence to the underlying model. In particular, the analysis reveals that both the Pr \rightarrow Pfr photoconversion and the Pfr \rightarrow Pr reversion can be driven by 2P absorption. The ratio of the rate constants for Pr \rightarrow Pfr and Pfr \rightarrow Pr 2P

conversion, k_1/k_{-1} , amounted to 0.55, 0.67, and 0.26 at 1190, 1250, and 1310 nm, respectively. Although smaller than the k_1/k_{-1} ratio of $0.69:0.31 = 2.2$ obtained for the photoreversible 1P conversion at 680 nm (see Fig. 1 c), we consider these values plausible. Notably, the k_1/k_{-1} ratios are directly reflected in the maximally attainable Pfr yields, which were lower for 2P conversion (see Fig. 4 d) than for 1P conversion (see Fig. 1 c).

Depending on wavelength, the 2P irradiation exhibited varying maximal Pfr yields. For a quantitative analysis, it is worth noting that the 2P focal volume had a depth of several millimeters and covered the entire path length of the sample cuvette (1 mm). Likewise, the 2P beam waist radius was around $130 \mu\text{m}$ and thus exceeded the $100 \mu\text{m}$ radius of the probe beam. Taken together, the absorbance measurements hence record the Pr and Pfr populations inside the 2P focal volume with negligible contribution of the surrounding bulk volume. In the range between 1170 and 1280 nm, up to 35–40% Pfr state was obtained inside the focal volume at the photostationary state. However, at 1310 nm, the attainable Pfr yield dropped to 25%, which could in principle be due to diminished Pr \rightarrow Pfr conversion, elevated Pfr \rightarrow Pr reversion, or both. Because these data mainly reflect the relative velocities of diffusion and the forward and reverse conversion rather than their absolute values, it is challenging to discriminate between these scenarios. That notwithstanding, our analyses implicate enhanced Pfr \rightarrow Pr reversion as the principal cause for the reduced Pfr yield at longer 2P wavelengths. These findings overall match those in the 1P regime, in which longer excitation wavelengths generally lead to smaller Pfr/Pr ratios at the photostationary state. However, whereas 1P irradiation with $(680 \pm 15) \text{ nm}$ effectively converted the *DdPCM* to the Pfr state (see Fig. 1 c), 2P irradiation at twice this wavelength did not (with, e.g., a Pfr yield of only 6% at 1370 nm). Intriguingly, the optimal range for photoconversion to the Pfr state in the 2P regime is thus shifted to slightly higher energies than expected based on photoconversion in the 1P regime (see Fig. 4 d). Notably, similar spectral shifts toward shorter wavelengths have been reported for the 2P excitation of several fluorescent proteins and have been attributed to non-Condon transitions (69–72). Regardless of the precise origin of the spectral shift, our data reveal that laser wavelengths between 1170 and 1300 nm achieve the best Pfr yield, thus informing the actuation of bacterial phytochromes by two-photon absorption.

Transcending earlier 2P fluorescence studies (28,73), we now demonstrate the actuation of bacterial phytochromes by 2P irradiation. Our analyses clearly show that 2P conversion of bacterial phytochromes is feasible in both the Pr \rightarrow Pfr and Pfr \rightarrow Pr directions, which paves the way toward novel applications in vivo. Notably, an assortment of optogenetic actuators based on bacterial phytochromes are already in place and can be deployed for the regulation of cellular processes including cyclic-nucleotide metabolism, gene

expression, and subcellular localization (10,31,74). Beyond affording superior spatial resolution, the 1.1–1.5 μm wavelengths used for 2P activation offer improved penetration through skull and bone (38). For practical application, however, water absorption, which increases by around 10-fold between 1 and 1.5 μm , needs to be taken into account (75). Taken together, the conversion of bacterial phytochromes by the near-infrared 2P illumination demonstrated here establishes a, to our knowledge, novel modality for specific, noninvasive intervention in the brain, complementing alternative approaches based on, for instance, optogenetics (7–9) and electrogenetics (76).

Q10

SUPPORTING MATERIAL

Supporting Material can be found online at <https://doi.org/10.1016/j.bpj.2021.01.028>.

AUTHOR CONTRIBUTIONS

E.U.R., S.G.S., and A.M. conceived the project. E.U.R., S.G.S., I.S., and A.M. supervised the work. D.G. and R.S. cloned, expressed, purified, and spectroscopically characterized phytochromes. E.A.Z., N.C., and A.G. performed two-photon conversion experiments. R.K.K. constructed the homology model and calculated 1P and 2P absorbance spectra; R.K.K. and I.S. analyzed the quantum chemical calculations. A.M. and E.A.Z. developed the analytical model for 2P excitation. A.M., E.U.R., S.G.S., E.A.Z., I.S., and R.K.K. interpreted the results. A.M., S.G.S., E.A.Z., E.U.R., R.K.K., and I.S. wrote the manuscript with input from all authors.

ACKNOWLEDGMENTS

This project has received funding from the European Union's H2020 FET OPEN NEUROPA project under the grant agreement no. 863214 (E.U.R., S.G.S., and A.M.). A.M. gratefully acknowledges funding by the Deutsche Forschungsgemeinschaft (grants MO2192/4-1 and MO2192/7-1). I.S. acknowledges funding by the European Research Council under the European Union's Horizon 2020 research and innovation program (grant no. 678169 "PhotoMutant"). I.S. thanks the SFB 1078 "Protonation Dynamics in Protein Function" for the Mercator fellowship. R.K.K. acknowledges support from the Lady Davis Trust for the Shunbrun postdoctoral fellowship. N.B.C. has received funding from the EU H2020 research and innovation program under the Marie Skłodowska-Curie (grant agreement no. 843801); E.A.Z. acknowledges funding by the Academy of Finland (grant 318281), RFBR (grant 20-08-01153\20), Russian Science Foundation (grant 20-75-00123), and the grant of the Russian Federation Government no. 075-15-2019-1877.

Q11

REFERENCES

- Hegemann, P. 2008. Algal sensory photoreceptors. *Annu. Rev. Plant Biol.* 59:167–189.
- Möglich, A., X. Yang, ..., K. Moffat. 2010. Structure and function of plant photoreceptors. *Annu. Rev. Plant Biol.* 61:21–47.
- Deisseroth, K., G. Feng, ..., M. J. Schnitzer. 2006. Next-generation optical technologies for illuminating genetically targeted brain circuits. *J. Neurosci.* 26:10380–10386.
- Nagel, G., D. Ollig, ..., P. Hegemann. 2002. Channelrhodopsin-1: a light-gated proton channel in green algae. *Science*. 296:2395–2398.

- Nagel, G., T. Szellas, ..., E. Bamberg. 2003. Channelrhodopsin-2, a directly light-gated cation-selective membrane channel. *Proc. Natl. Acad. Sci. USA*. 100:13940–13945.
- Losi, A., K. H. Gardner, and A. Möglich. 2018. Blue-light receptors for optogenetics. *Chem. Rev.* 118:10659–10709.
- Klapoetke, N. C., Y. Murata, ..., E. S. Boyden. 2014. Independent optical excitation of distinct neural populations. *Nat. Methods*. 11:338–346.
- Oda, K., J. Vierock, ..., O. Nureki. 2018. Crystal structure of the red light-activated channelrhodopsin Chrimson. *Nat. Commun.* 9:3949.
- Gong, X., D. Mendoza-Halliday, ..., G. Feng. 2020. An ultra-sensitive step-function opsin for minimally invasive optogenetic stimulation in mice and macaques. *Neuron*. 107:38–51.e8.
- Gourinchas, G., S. Etlz, and A. Winkler. 2019. Bacteriophytochromes - from informative model systems of phytochrome function to powerful tools in cell biology. *Curr. Opin. Struct. Biol.* 57:72–83.
- Weissleder, R. 2001. A clearer vision for *in vivo* imaging. *Nat. Biotechnol.* 19:316–317.
- Butler, W. L., K. H. Norris, ..., S. B. Hendricks. 1959. Detection, assay, and preliminary purification of the pigment controlling photoresponsive development of plants. *Proc. Natl. Acad. Sci. USA*. 45:1703–1708.
- Rockwell, N. C., and J. C. Lagarias. 2010. A brief history of phytochromes. *ChemPhysChem*. 11:1172–1180.
- Rockwell, N. C., and J. C. Lagarias. 2020. Phytochrome evolution in 3D: deletion, duplication, and diversification. *New Phytol.* 225:2283–2300.
- Möglich, A., R. A. Ayers, and K. Moffat. 2009. Structure and signaling mechanism of Per-ARNT-Sim domains. *Structure*. 17:1282–1294.
- Aravind, L., and C. P. Ponting. 1997. The GAF domain: an evolutionary link between diverse phototransducing proteins. *Trends Biochem. Sci.* 22:458–459.
- Yang, X., J. Kuk, and K. Moffat. 2008. Crystal structure of *Pseudomonas aeruginosa* bacteriophytochrome: photoconversion and signal transduction. *Proc. Natl. Acad. Sci. USA*. 105:14715–14720.
- Essen, L. O., J. Mailliet, and J. Hughes. 2008. The structure of a complete phytochrome sensory module in the Pr ground state. *Proc. Natl. Acad. Sci. USA*. 105:14709–14714.
- Takala, H., A. Björling, ..., S. Westenhoff. 2014. Signal amplification and transduction in phytochrome photosensors. *Nature*. 509:245–248.
- Burgie, E. S., J. Zhang, and R. D. Vierstra. 2016. Crystal structure of Deinococcus phytochrome in the photoactivated state reveals a cascade of structural rearrangements during photoconversion. *Structure*. 24:448–457.
- Möglich, A. 2019. Signal transduction in photoreceptor histidine kinases. *Protein Sci.* 28:1923–1946.
- Ni, M., J. M. Tepperman, and P. H. Quail. 1998. PIF3, a phytochrome-interacting factor necessary for normal photoinduced signal transduction, is a novel basic helix-loop-helix protein. *Cell*. 95:657–667.
- Pham, V. N., P. K. Kathare, and E. Huq. 2018. Phytochromes and phytochrome interacting factors. *Plant Physiol.* 176:1025–1038.
- Golonka, D., P. Fischbach, ..., A. Möglich. 2019. Deconstructing and repurposing the light-regulated interplay between *Arabidopsis* phytochromes and interacting factors. *Commun. Biol.* 2:448.
- Golonka, D., U. Gerken, ..., A. Möglich. 2020. The association kinetics encode the light dependence of arabidopsis phytochrome B interactions. *J. Mol. Biol.* 432:4327–4340.
- Gasser, C., S. Taiber, ..., A. Möglich. 2014. Engineering of a red-light-activated human cAMP/cGMP-specific phosphodiesterase. *Proc. Natl. Acad. Sci. USA*. 111:8803–8808.
- Stüven, B., R. Stabel, ..., A. Möglich. 2019. Characterization and engineering of photoactivated adenylyl cyclases. *Biol. Chem.* 400:429–441.
- Piatkevich, K. D., F. V. Subach, and V. V. Verkhusha. 2013. Engineering of bacterial phytochromes for near-infrared imaging, sensing, and light-control in mammals. *Chem. Soc. Rev.* 42:3441–3452.

29. Ryu, M.-H., I.-H. Kang, ..., M. Gomelsky. 2014. Engineering adenylate cyclases regulated by near-infrared window light. *Proc. Natl. Acad. Sci. USA*. 111:10167–10172.
30. Ettl, S., R. Lindner, ..., A. Winkler. 2018. Structure-guided design and functional characterization of an artificial red light-regulated guanylate/adenylate cyclase for optogenetic applications. *J. Biol. Chem.* 293:9078–9089.
31. Shcherbakova, D. M., A. A. Shemetov, ..., V. V. Verkhusha. 2015. Natural photoreceptors as a source of fluorescent proteins, biosensors, and optogenetic tools. *Annu. Rev. Biochem.* 84:519–550.
32. Ziegler, T., and A. Möglich. 2015. Photoreceptor engineering. *Front. Mol. Biosci.* 2:30.
33. Filonov, G. S., K. D. Piatkevich, ..., V. V. Verkhusha. 2011. Bright and stable near-infrared fluorescent protein for in vivo imaging. *Nat. Biotechnol.* 29:757–761.
34. Ryu, M.-H., and M. Gomelsky. 2014. Near-infrared light responsive synthetic c-di-GMP module for optogenetic applications. *ACS Synth. Biol.* 3:802–810.
35. Stabel, R., B. Stüven, ..., A. Möglich. 2019. Revisiting and redesigning light-activated cyclic-monomonucleotide phosphodiesterases. *J. Mol. Biol.* 431:3029–3045.
36. Kaberniuk, A. A., A. A. Shemetov, and V. V. Verkhusha. 2016. A bacterial phytochrome-based optogenetic system controllable with near-infrared light. *Nat. Methods*. 13:591–597.
37. Redchuk, T. A., A. A. Kaberniuk, and V. V. Verkhusha. 2018. Near-infrared light-controlled systems for gene transcription regulation, protein targeting and spectral multiplexing. *Nat. Protoc.* 13:1121–1136.
38. Golovynskyi, S., I. Golovynska, ..., T. Y. Ohulchanskyy. 2018. Optical windows for head tissues in near-infrared and short-wave infrared regions: approaching transcranial light applications. *J. Biophotonics*. 11:e201800141.
39. Bashkatov, A. N., E. A. Genina, ..., V. V. Tuchin. 2006. Optical properties of human cranial bone in the spectral range from 800 to 2000 nm. *In Saratov Fall Meeting 2005: Optical Technologies in Biophysics and Medicine VII. International Society for Optics and Photonics*, p. 616310.
40. Hong, G., S. Diao, ..., H. Dai. 2014. Through-skull fluorescence imaging of the brain in a new near-infrared window. *Nat. Photonics*. 8:723–730.
41. Piatkevich, K. D., H.-J. Suk, ..., V. V. Verkhusha. 2017. Near-infrared fluorescent proteins engineered from bacterial phytochromes in neuroimaging. *Biophys. J.* 113:2299–2309.
42. Forli, A., D. Vecchia, ..., T. Fellin. 2018. Two-photon bidirectional control and imaging of neuronal excitability with high spatial resolution In Vivo. *Cell Rep.* 22:3087–3098.
43. Dal Maschio, M., J. C. Donovan, ..., H. Baier. 2017. Linking neurons to network function and behavior by two-photon holographic optogenetics and volumetric imaging. *Neuron*. 94:774–789.e5.
44. Yang, W., L. Carrillo-Reid, ..., R. Yuste. 2018. Simultaneous two-photon imaging and two-photon optogenetics of cortical circuits in three dimensions. *eLife*. 7:e32671.
45. Prakash, R., O. Yizhar, ..., K. Deisseroth. 2012. Two-photon optogenetic toolbox for fast inhibition, excitation and bistable modulation. *Nat. Methods*. 9:1171–1179.
46. Gibson, D. G., L. Young, ..., H. O. Smith. 2009. Enzymatic assembly of DNA molecules up to several hundred kilobases. *Nat. Methods*. 6:343–345.
47. Mukougawa, K., H. Kanamoto, ..., T. Kohchi. 2006. Metabolic engineering to produce phytochromes with phytochromobilin, phycocyanobilin, or phycoerythrobilin chromophore in *Escherichia coli*. *FEBS Lett.* 580:1333–1338.
48. Berkelman, T. R., and J. C. Lagarias. 1986. Visualization of bilin-linked peptides and proteins in polyacrylamide gels. *Anal. Biochem.* 156:194–201.
49. Butler, W. L., S. B. Hendricks, and H. W. Siegelman. 1964. Actin spectra of phytochrome in vitro. *Photochem. Photobiol.* 3:521–528.
50. Möglich, A. 2018. An open-source, cross-platform resource for nonlinear least-squares curve fitting. *J. Chem. Educ.* 95:2273–2278.
51. Waterhouse, A., M. Bertoni, ..., T. Schwede. 2018. SWISS-MODEL: homology modelling of protein structures and complexes. *Nucleic Acids Res.* 46:W296–W303.
52. Burgie, E. S., T. Wang, ..., R. D. Vierstra. 2014. Crystallographic and electron microscopic analyses of a bacterial phytochrome reveal local and global rearrangements during photoconversion. *J. Biol. Chem.* 289:24573–24587.
53. Hintze, B. J., S. M. Lewis, ..., D. C. Richardson. 2016. Molprobity's ultimate rotamer-library distributions for model validation. *Proteins*. 84:1177–1189.
54. Williams, C. J., J. J. Headd, ..., D. C. Richardson. 2018. MolProbity: more and better reference data for improved all-atom structure validation. *Protein Sci.* 27:293–315.
55. Lu, Y., M. R. Farrow, ..., T. W. Keal. 2019. Open-Source, python-based redevelopment of the ChemShell multiscale QM/MM environment. *J. Chem. Theory Comput.* 15:1317–1328.
56. Maier, J. A., C. Martinez, ..., C. Simmerling. 2015. ff14SB: improving the accuracy of protein side chain and backbone parameters from ff99SB. *J. Chem. Theory Comput.* 11:3696–3713.
57. Wiebeler, C., and I. Schapiro. 2019. QM/MM benchmarking of cyanobacteriochrome Slr1393g3 absorption spectra. *Molecules*. 24:1720.
58. Balasubramani, S. G., G. P. Chen, ..., J. M. Yu. 2020. TURBOMOLE: modular program suite for ab initio quantum-chemical and condensed-matter simulations. *J. Chem. Phys.* 152:184107.
59. Beerepoot, M. T. P., D. H. Friese, ..., K. Ruud. 2015. Benchmarking two-photon absorption cross sections: performance of CC2 and CAM-B3LYP. *Phys. Chem. Chem. Phys.* 17:19306–19314.
60. Yeh, K.-C., S.-H. Wu, ..., J. C. Lagarias. 1997. A cyanobacterial phytochrome two-component light sensory system. *Science*. 277:1505–1508.
61. Hughes, J., T. Lamparter, ..., T. Börner. 1997. A prokaryotic phytochrome. *Nature*. 386:663.
62. Davis, S. J., A. V. Vener, and R. D. Vierstra. 1999. Bacteriophytochromes: phytochrome-like photoreceptors from nonphotosynthetic eubacteria. *Science*. 286:2517–2520.
63. Bhoo, S.-H., S. J. Davis, ..., R. D. Vierstra. 2001. Bacteriophytochromes are photochromic histidine kinases using a biliverdin chromophore. *Nature*. 414:776–779.
64. Wagner, J. R., J. S. Brunzelle, ..., R. D. Vierstra. 2005. A light-sensing knot revealed by the structure of the chromophore-binding domain of phytochrome. *Nature*. 438:325–331.
65. Multamäki, E., R. Nanekar, ..., H. Takala. 2020. Illuminating a phytochrome paradigm – a light-activated phosphatase in two-component signaling uncovered. *bioRxiv* <https://doi.org/10.1101/2020.06.26.173310>.
66. Wiebeler, C., A. G. Rao, ..., I. Schapiro. 2019. The effective conjugation length is responsible for the red/green spectral tuning in the cyanobacteriochrome Slr1393g3. *Angew. Chem. Int.Engl.* 58:1934–1938.
67. Church, J. R., A. G. Rao, ..., I. Schapiro. Computational studies of photochemistry in phytochrome proteins. In *QM/MM Studies of Light-responsive Biological Systems*, T. Andrúniów, M. Olivucci, eds. (Springer), pp. 197–226.
68. Grabarek, D., and T. Andrúniów. 2019. Assessment of functionals for TDDFT calculations of one- and two-photon absorption properties of neutral and anionic fluorescent proteins chromophores. *J. Chem. Theory Comput.* 15:490–508.
69. Hosoi, H., S. Yamaguchi, ..., T. Tahara. 2008. Hidden electronic excited state of enhanced green fluorescent protein. *J. Phys. Chem. B*. 112:2761–2763.
70. Drobizhev, M., S. Tillo, ..., A. Rebane. 2009. Absolute two-photon absorption spectra and two-photon brightness of orange and red fluorescent proteins. *J. Phys. Chem. B*. 113:855–859.

71. Kamarchik, E., and A. I. Krylov. 2011. Non-condon effects in the one- and two-photon absorption spectra of the green fluorescent protein. *J. Phys. Chem. Lett.* 2:488–492.
72. Homans, R. J., R. U. Khan, ..., A. R. Jones. 2018. Two photon spectroscopy and microscopy of the fluorescent flavoprotein, iLOV. *Phys. Chem. Chem. Phys.* 20:16949–16955.
73. Piatkevich, K. D., F. V. Subach, and V. V. Verkhusha. 2013. Far-red light photoactivatable near-infrared fluorescent proteins engineered from a bacterial phytochrome. *Nat. Commun.* 4:2153.
74. Shcherbakova, D. M., O. V. Stepanenko, ..., V. V. Verkhusha. 2018. Near-infrared fluorescent proteins: multiplexing and optogenetics across scales. *Trends Biotechnol.* 36:1230–1243.
75. Hale, G. M., and M. R. Querry. 1973. Optical constants of water in the 200-nm to 200-microm wavelength region. *Appl. Opt.* 12:555–563.
76. Krawczyk, K., S. Xue, ..., M. Fussenegger. 2020. Electrogenetic cellular insulin release for real-time glycemic control in type 1 diabetic mice. *Science.* 368:993–1001.